Supporting Information

Band Gap Engineering with Ultralarge Biaxial Strains in Suspended Monolayer MoS_2

David Lloyd [1], Xinghui Liu[2], Jason W. Christopher[3], Lauren Cantley[1], Anubhav Wadehra[4], Brian L. Kim[1], Bennett B. Goldberg[3], Anna K. Swan[5], and J. Scott Bunch[1,6*]

[1]Boston University, Department of Mechanical Engineering, Boston, MA 02215 USA

[2]University of Colorado, Department of Mechanical Engineering, Boulder, CO 80309 USA

[3]Department of Physics, Boston University, 590 Commonwealth Avenue, Boston, Massachusetts 02215, United States

[4]Department of Materials and Metallurgy, PEC University of Technology, Chandigarh, India-160012

[5]Department of Electrical and Computer Engineering, Boston University, 590 Commonwealth Avenue, Boston, Massachusetts 02215, United States

[6]Boston University, Division of Materials Science and Engineering, Brookline, MA 02446 USA

*e-mail: bunch@bu.edu, fax: 1-617-353-5866

1. CVD growth

To grow highly impermeable monolayer MoS_2, we use a modified version of the growth method described in Ref 1. A powder source of MoS_2 is placed in the center of a furnace, and a SiO_x substrate is placed in a cooler region downstream. The system is pumped down to 10 mTorr to remove any contaminating gases after which we flow 60 sccm Ar as a carrier gas, plus 0.1 sccm of O_2 and 1 sccm of H_2 gas. The furnace is heated to 900 ^oC and held at that temperature for 15 minutes after which it is left to cool naturally to room temperature.

The process described in Ref. 1 depends on the sublimation of MoS_2 at the hottest part of the furnace which is carried downstream and condenses on the substrate in a cooler region. We found that the yield could be considerably improved by the addition of small amounts of oxygen and hydrogen. This led to large monolayer coverage with triangular sheets with a side length as large as 150 μm. The likely mechanism for this growth is that the O_2 reacts to form either MoO_2 or MoO_3, thus liberating 2S. These molecules then flow downstream to react on the surface of the substrate. This method is therefore analogous to several other methods in the literature[2], in which a molybdenum oxide and sulfur powder precursors are used. However, we found our method to give a considerably larger and more reliable yield of impermeable MoS_2 membranes.

2. Optical measurements and multilayer characterization

For PL and Raman measurements, we used 600 l/mm and 2400 l/mm gratings respectively. Laser powers were kept below 10 $\mu W/m^2$ to avoid heating effects, which can modify the PL peak positions or open permeable holes in the membranes. We found our unstrained suspended MoS_2 membranes had a high intensity A peak at ~1.88 eV in the PL spectrum, and a Raman mode peak separation of ~19 cm^{-1} which confirms that our samples were of a monolayer thickness.

PL and Raman measurements were also used to confirm the thickness of our bilayer and trilayer samples (inset Fig. S1). Our multilayer samples were prepared by mechanical exfoliation so the stacking orientation between the layers was not controlled; however the Raman peak separations for our bilayer and trilayer samples were 21.7 cm^{-1} and 23.7 cm^{-1} respectively, which are consistent with exfoliated samples in previous reports[3].

Thickness	E^1_{2g} mode shift rate (cm^{-1} / %)	A_{1g} mode shift rate (cm^{-1} / %)
Monolayer	-5.2	-1.7
Bilayer	-4.2	-1.3
Trilayer	-3.0	-0.7

Table S1. Raman mode shift rates for each membrane thickness.

A comparison of the strain dependencies of the Raman modes that we observed in Fig. 2c of the main text is presented in Table S1. These results show that both modes are less strain sensitive with increasing membrane thickness, an effect which was also observed in Ref 4. We also plot the ratio of the integrated intensities of the two Raman modes (E^1_{2g}/A_{1g}) in Fig. S1. All three thicknesses have approximately the same E^1_{2g}/A_{1g} at zero strain, and each show some small increase in this ratio with strain.

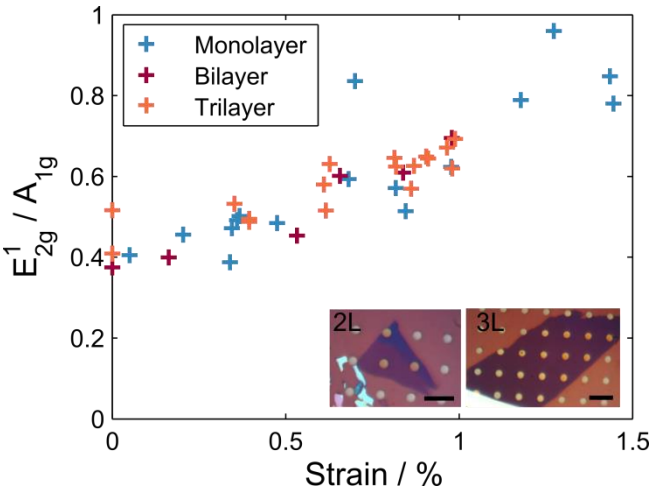

Figure S1. The ratio of integrated intensities of the E^1_{2g} to A_{1g} Raman modes for different membrane thicknesses. Scale bars are 15 µm.

3. Pressurization

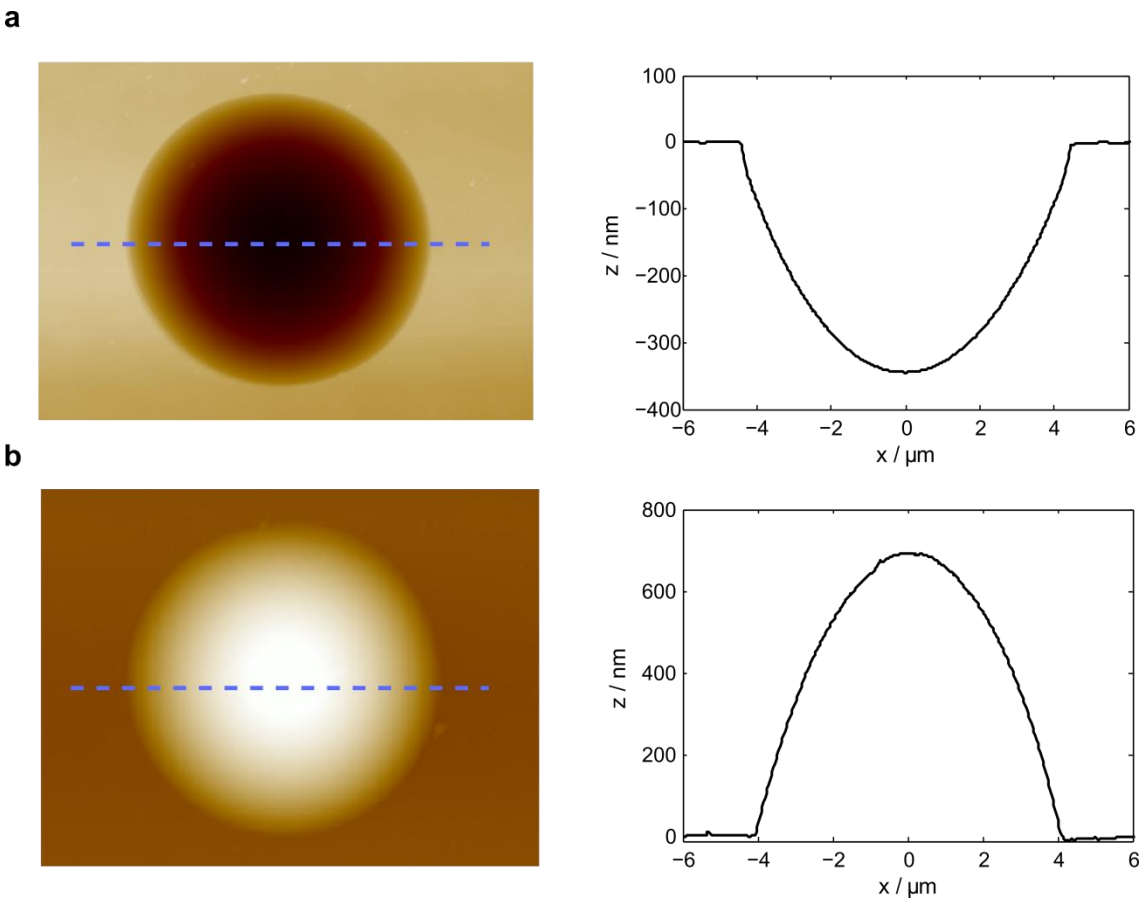

Figure S2. AFM images and cross sections of a) a device with p_{int} = 0 and b) a device with p_{int} ~ 0.75 MPa. In both a) and b) p_{ext} = 1 atm.

The devices used to collect data in Fig. 3 of the main text had p_{int} = 0 by leaving them to equilibrate in a vacuum chamber for several days. The only exception to this was for the data points at Δp =0, which were taken by inflating the devices with gas until p_{int} = 1 atm and the membranes were unstrained. Fig. S2a shows an AFM image and cross section of such a device at p_{ext} = 1 atm and p_{int} = 0 so that Δp < 0. This image was taken immediately after the device had been exposed to p_{ext} ~1380 kPa for several hours, demonstrating that very little gas leaked into the device cavities during that time. Fig. S2b is an image of one of the CVD devices used to take Raman and PL data in Fig. 2 of the main text where p_{ext} = 1 atm and p_{int} ~ 0.75 MPa so that Δp > 0.

4. Gas permeance

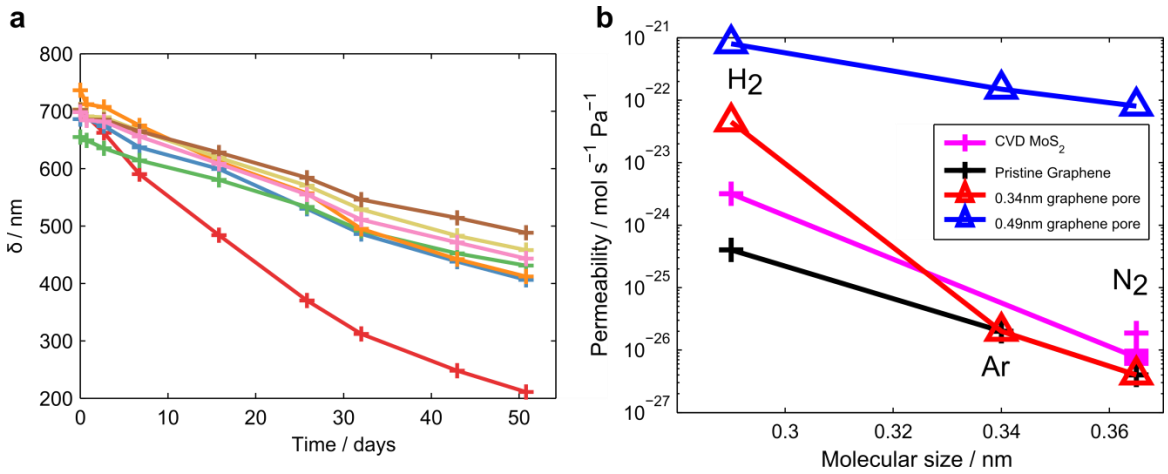

Figure S3. a) Seven different CVD MoS_2 devices pressurized with nitrogen and deflating over time. b) Comparison of CVD MoS_2 with pristine and etched graphene.

The permeability of our CVD MoS_2 membranes can be quantified by measuring the rate at which gas leaks out of the pressurized micro-cavities. To do this, we follow the method used in Ref 5. Briefly, we assume that the leak rate of number of moles of gas n can be written in terms of permeability k and the pressure difference across the membrane Δp as,

$$\frac{dn}{dt} = -k\Delta p \qquad (1)$$

Using the ideal gas law, we can determine dn/dt and Δp in terms of the maximum deflection of the membrane bulge δ. In this way, we can determine k by taking AFM measurements of δ over time as devices pressurized with various gases deflate. Fig. S3a shows how δ changes as seven CVD MoS_2 devices initially pressurized with N_2 gas deflate over time, and shows that it takes several months for most devices to fully deflate. We can compare the permeability k for these membranes with graphene devices in the same geometry for gases of varying molecular size in Fig. S2b. The graphene data was taken from Ref 6. For both nitrogen and hydrogen, the permeability of the MoS_2 is higher than for pristine graphene, however orders of magnitude less than a graphene membrane with an estimated 0.49 nm pore. We can therefore conclude that our CVD membranes must be completely free of permeable nanometer scale vacancies.

5. Hencky's solution for the uniform lateral loading of circular membranes.

The mechanics of a uniform pressure on an atomically thin membrane over a cylindrical cavity is described in detail elsewhere[7,8], and this discussion closely follows Fichter (1997). Briefly, by assuming the uniform lateral loading of the membrane, the governing equations can be written in terms of radius *r* and pressure difference Δp as,

$$\sigma_r \frac{dw}{dr} = -\frac{\Delta p r}{2} \tag{2}$$

$$\sigma_\theta = \frac{d}{dr}(r\sigma_r) \tag{3}$$

with the linear stress-strain relationship,

$$\sigma_\theta - \upsilon\sigma_r = Et\varepsilon_\theta \tag{4}$$

The radial stress, σ_r and the vertical deflection *w* can be expanded as an infinite series of even powers of radius *r*, and their exact form can be determined by solving for S2 and S3. The final expression for biaxial strain is then written as,

$$\varepsilon_b = \left(\frac{\delta}{a}\right)^2 \frac{b_0(\upsilon)(1-\upsilon)K(\upsilon)^{2/3}}{4} \tag{5}$$

in terms of two numerical constants b_0 and *K* which both depend only on Poisson's ratio υ. For υ = 0.29, *K* = 3.54 and b_0 = 1.72, which gives the value of σ = 0.709 used in the main text.

6. Sliding and Repeatability

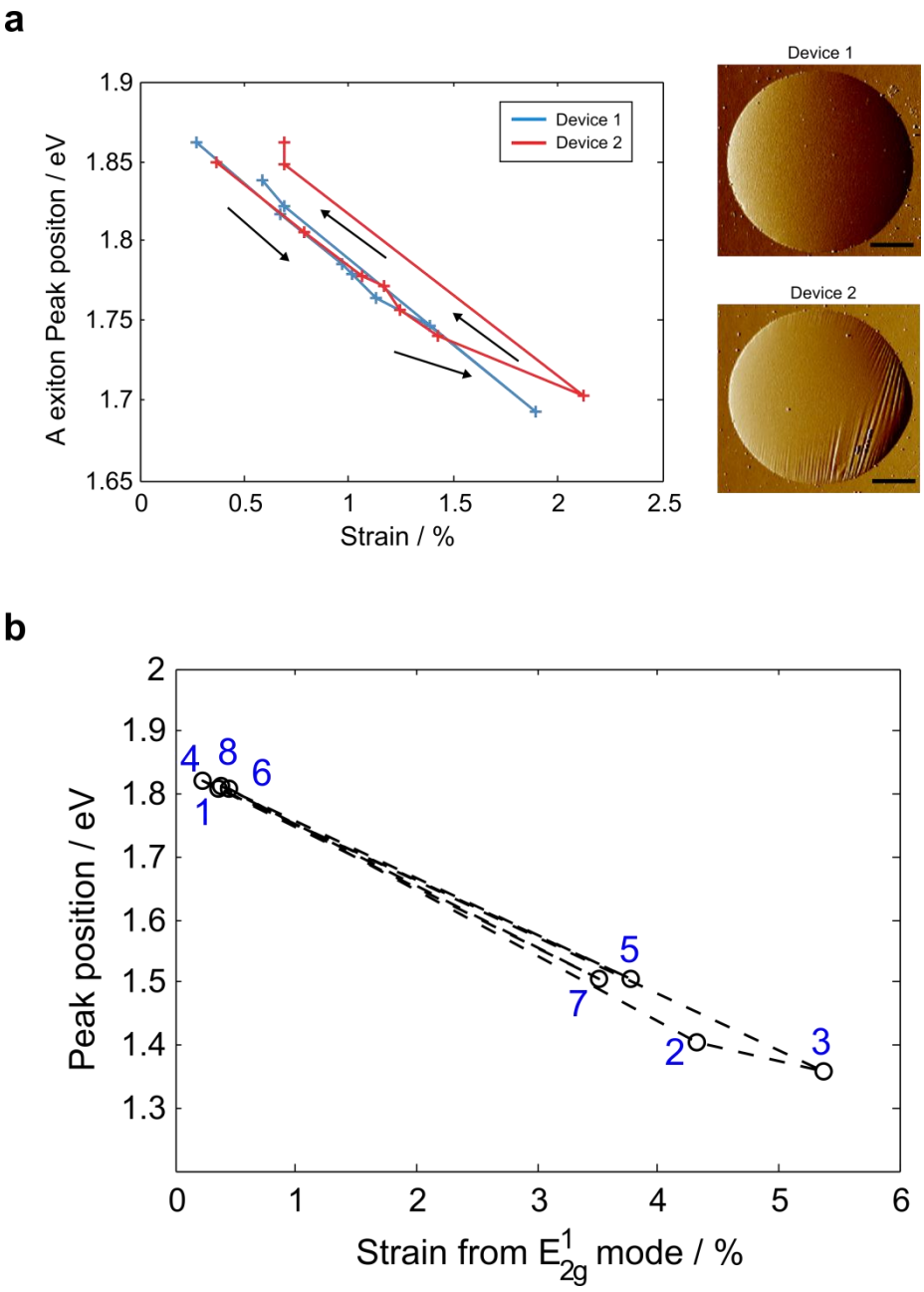

Figure S4. a) An example of the peak shift in two monolayer devices in which p_{int} was increased then decreased, with AFM images of both devices after pressure cycling (scale bars are 2 μm). Device 2 shows evidence of slipping. b) The repeatability of subjecting a device to high strain. Measurements were taken in the sequence indicated.

Under high strains our devices may be forced to slide over the substrate, an effect which has been observed in graphene[9]. This sliding would allow the membrane deflection δ to increase,

and thus cause us to over-estimate the strain from our AFM measurements. To see if sliding has occurred, we plot the relationship between strain and the *A* peak position during the initial increase in internal pressures followed by the deflation of devices (Fig. S4). Device 1 shows little hysteresis, however Device 2 shows evidence of significant sliding. This can further be confirmed by the AFM images of the devices after deflating, with Device 2 showing wrinkling which was not previously present. To avoid any influence of this effect on our data presented in Fig. 2 of the main text, we only used data taken from devices which showed none of these signs of sliding.

7. Decrease in the *A* exciton intensity - comparison to theoretical predictions.

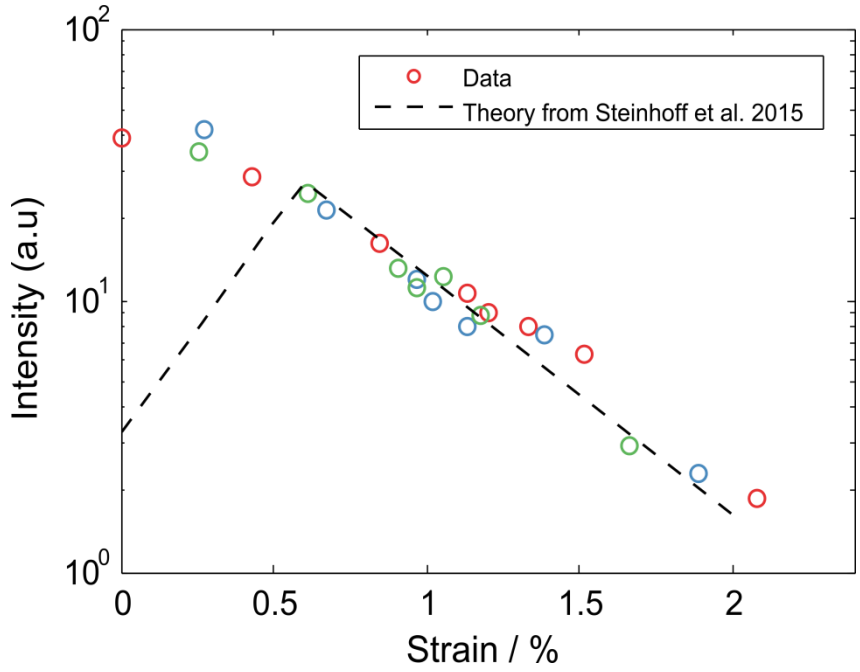

Figure S5. Comparison of the change in *A* peak exciton intensity with strain to a theoretical prediction. The intensity of our data has been scaled for comparison with the theory.

The exponential decrease in *A* peak intensity shown in Fig 2a inset of the main text compares well to the theory described in Steinhoff et al. at large strains (Fig. S5). At strains below 0.5 % however, they predicted that the PL intensity would increase with strain, caused by changes in conduction band minima at the Σ point of the conduction band. We did not observe such an enhancement over this range, however the difference may be due to different estimates of the doping level in the theory and the true doping level in our devices.

8. Interference effects

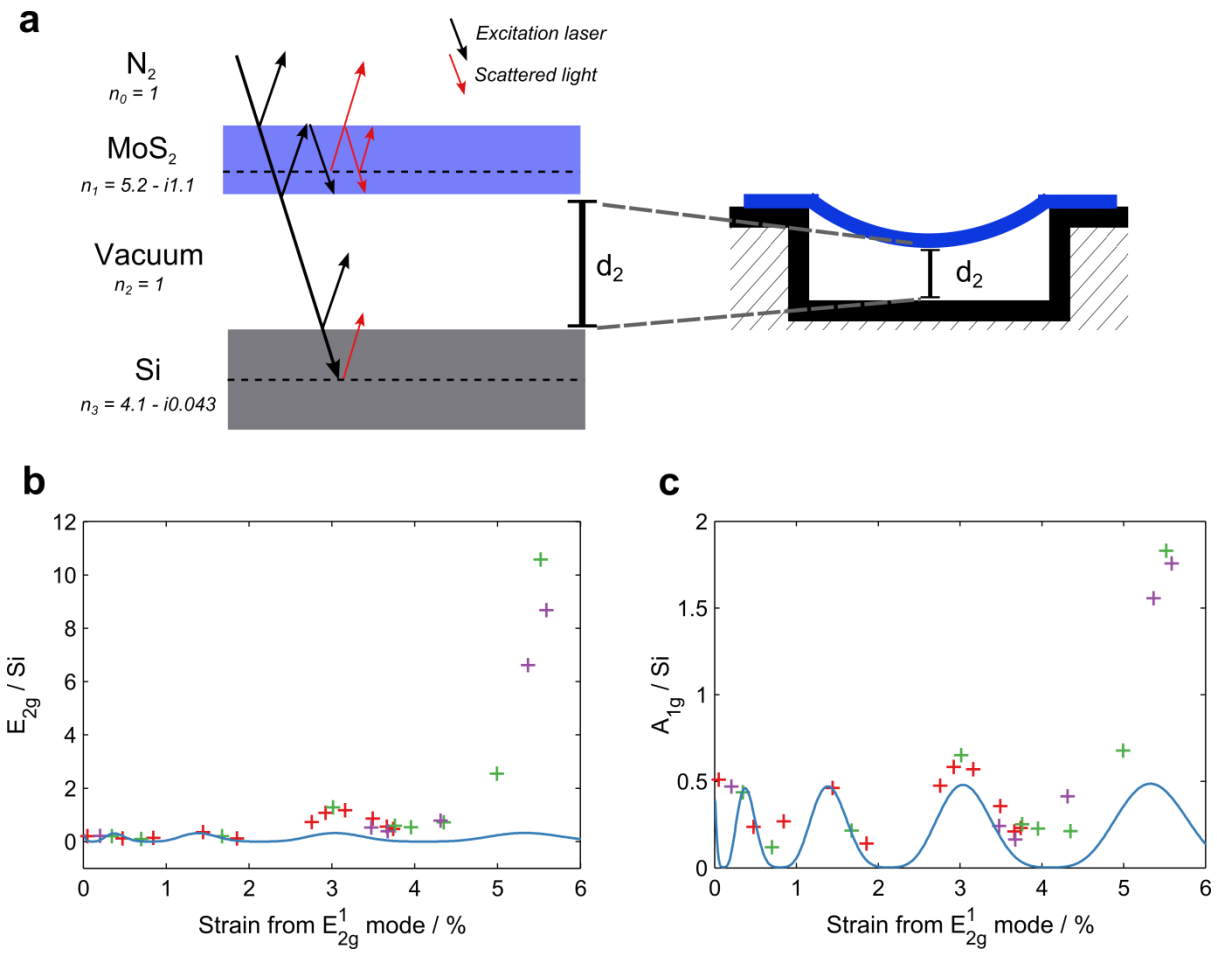

Figure S6. a) A ray diagram of incident and scattered light. The effective power of the excitation laser (black) is the sum of the incident beam with its reflected beams. The intensities of Raman scattered light (red) also depend on the sum of reflected rays, and rays scattered at different phases within the MoS_2 or Si. The effect of this interference for each frequency of light depends on the distance between membrane and substrate, d_2, which changes as the devices are strained. b) & c) The intensities of the E^1_{2g} and A_{1g} peaks relative to the Si peak. We compare our data (crosses) to the interference model (blue line).

The interference between light scattered of the MoS_2 membrane and the silicon at the bottom of the well may affect the relative intensities of the A_{1g} and E^1_{2g} modes (Fig S6a). To rule this out as the cause of our observed changes to Raman mode intensities, we closely follow a model developed in other works[10,11], originally used to determine the effect of the substrate thickness on the Raman mode intensities. In our case, instead of a layer of SiO_2, we have a vacuum cavity of distance d_2 which changes as the device bulges down under high pressures.

Using the Fresnel equations, we can deduce the change in intensity of each MoS_2 Raman mode relative to the Si peak, as d_2 decreases from its unstrained value of 1.5 μm (equivalent to the depth of the well) with increasing strain. We deduce the value of d_2 by using the Hencky model described in the main text, which can be used to convert strain we determined from the E^1_{2g} peak position, to a membrane deflection δ. d_2 is then equal to the difference between δ and the well depth. We also account for the strain induced shift of each mode in these calculations, which makes the wavelength of the scattered light also dependent on strain.

The model is plotted against our data in Fig. S6b & Fig. S6c, and the intensity of the model curve is scaled in order to be in coincidence with our data at low strains. We find both the E^1_{2g} and A_{1g} peak intensities increase beyond what is expected from the interference model at high strains. We therefore conclude that the observed increase in both Raman mode intensities at high strain was not due to the effect of interference, but was rather an intrinsic property of the material under strain. Similarly, the interference model does not account for why the ratio E^1_{2g}/ A_{1g} increases so dramatically. As the Raman modes are so similar in energy, interference effects should cause less than a 10% change in this ratio, and so we conclude that this is also strain induced effect.

9. Additional Raman data

We plot the ratio of the Raman modes E^1_{2g}/ A_{1g} against strain (Fig. S7a), and at the highest strains there is a ten-fold enhancement of this ratio. To further confirm that the changes in this ratio were not due to the changing distance d_2, we also plot the data taken from our bulged up devices. Despite having a different well depth, and a d_2 which was increasing with strain (rather than decreasing), the data from the bulged up devices shows a similar trend to that of the bulged down devices. This is further evidence that this ratio change was not caused by interference.

In Fig. S7b we show a zoomed in version of the data presented in Fig. 3b of the main text, in order to show the shift of second order peaks with strain. In the unstrained membrane, this feature is centered around 455 cm^{-1}, and we therefore identify it as the 2LA(M) feature[12]. This feature is very strain sensitive, and shifts down to ~415 at 5.5% strain. Like the other peaks its intensity increases with strain, which is further evidence that our laser line is crossing a resonance.

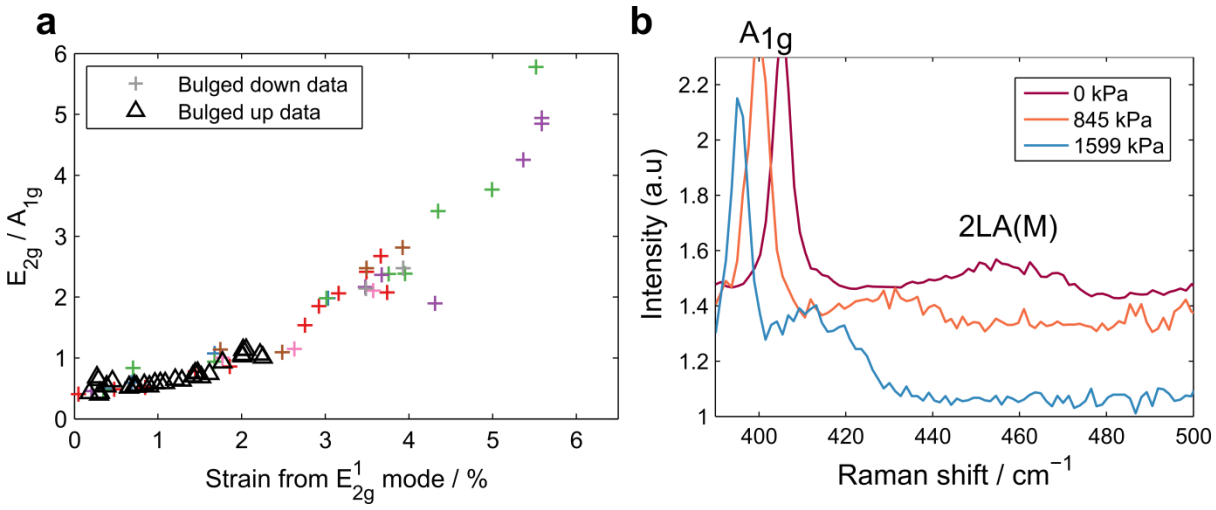

Figure S7. a) The Raman intensity ratio E^1_{2g}/ A_{1g} for bulged up (black triangles) and bulged down (colored crosses) devices. b) A zoomed in version of Fig. 3b of the main text to highlight the 2LA(M) mode.

Finally, we did a line scan of a device with Δp = 1599 kPa, corresponding to a biaxial strain at the center of the device of ~5.6 % (Fig S8a). As strain increases in our devices, the curvature of the membranes also increases. As our laser spot has a finite size, this change in curvature would change the angle between the incident light and the membrane. To rule this out as a cause of the change in Raman mode intensities, we plot the intensities of the Raman modes as a function of distance *x* across the device. If changes in angle between laser light and membrane were causing increases in Raman intensity, we would expect the largest change to occur at the edge of the membrane, where the angle change would be the most. However, Fig. S8c and Fig. S8d show that this is not the case. Intensities of both Raman modes and the ratio E^1_{2g}/ A_{1g} are both largest in the center of the device, where the biaxial strain is the most and the membrane is closest to being flat. We therefore rule out the device curvature as the cause of these intensity changes.

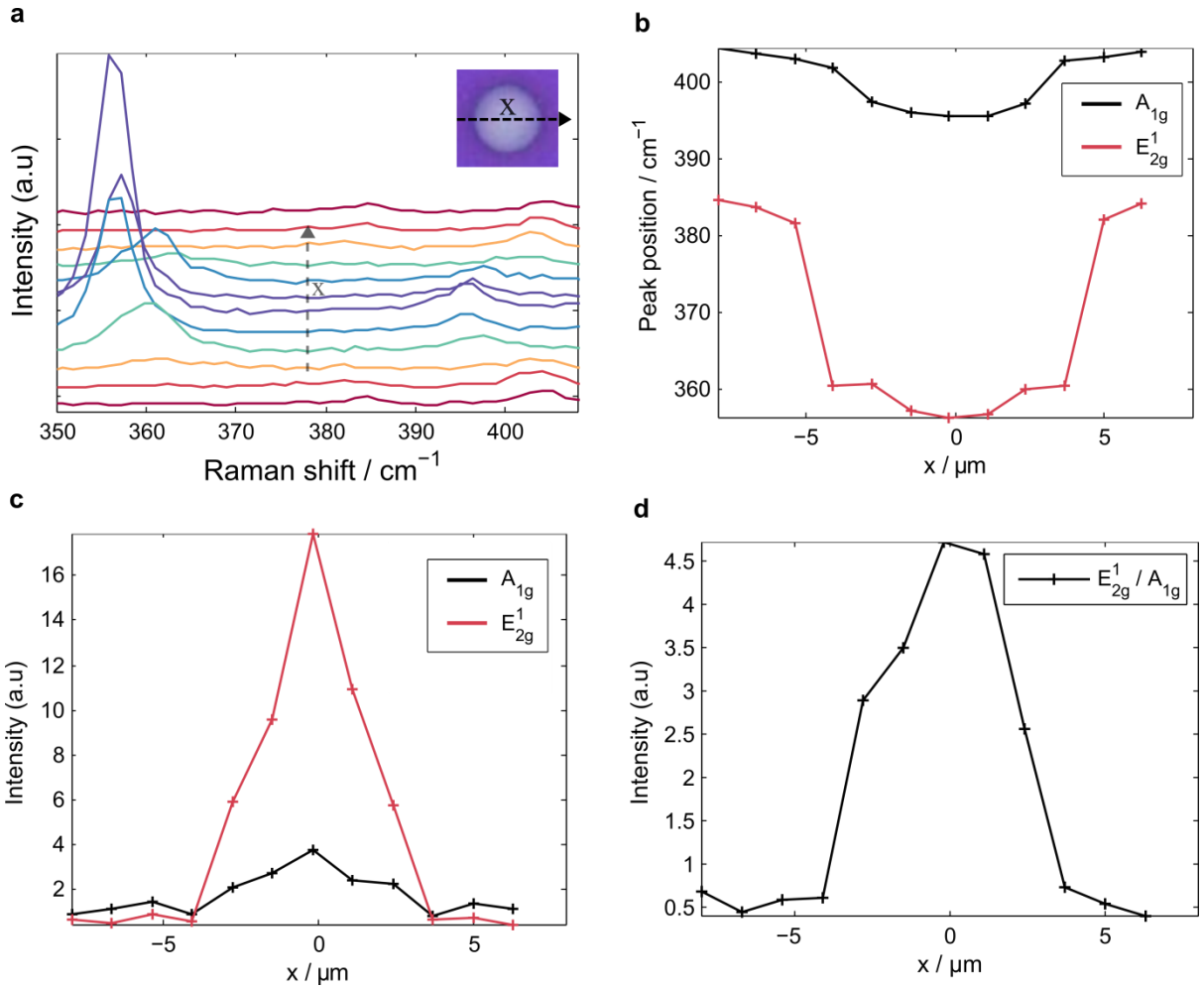

Figure S8. a) Line scan of Raman modes across a device. b) Peak positions and c) peak intensities of the Raman modes (normalized to the Si peak) across the device. d) The ratio E^1_{2g} / A_{1g} of the two Raman mode intensities across the device.

10. Additional PL data

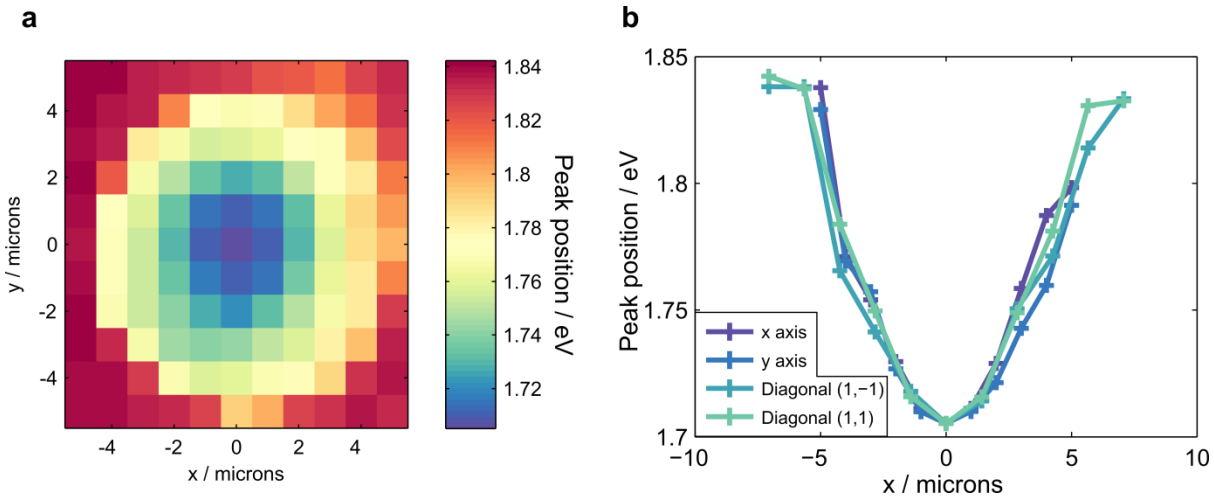

Figure S9. a) A PL map of a device with p_{int} ~ 0.75 MPa and p_{ext} = 1 atm, with colors representing the A peak position. b) Line cuts through the center of the device along the x, y, (1,1) and (1,-1) directions.

The inhomogeneous strain field we apply across our devices should produce a spatially varying optical band gap. To confirm this, we took a PL map of a strained device and plotted the peak position of the A peak at each pixel in Fig. S9a. We also plot line cuts through the center of the device along the axial and diagonal directions (Fig. S9b). The band gap is redshifted to ~1.7 eV at the center of the device where the membrane is subject to a pure biaxial strain. Around the edge of the device the strain becomes approximately uniaxial along the radial direction, which results in a lower band gap shift due to the smaller uniaxial band gap tuning rate in MoS_2. These results demonstrate that our device geometry produces an energy gradient which could allow excitons produced around the edge of the device to be funneled towards the lower energy region at the center of the device[13].

References

(1) Wu, S.; Huang, C.; Aivazian, G.; Ross, J. S.; Cobden, D. H. *ACS Nano* **2013**, *7* (3), 2768–2772.

(2) van der Zande, A. M.; Huang, P. Y.; Chenet, D. a; Berkelbach, T. C.; You, Y.; Lee, G.-H.; Heinz, T. F.; Reichman, D. R.; Muller, D. A; Hone, J. *Nat. Mater.* **2013**, *12* (6), 554–561.

(3) Lee, C.; Yan, H.; Brus, L. E.; Heinz, T. F.; Hone, J.; Ryu, S. *ACS Nano* **2010**, *4* (5), 2695–2700.

(4) Rice, C.; Young, R. J.; Zan, R.; Bangert, U.; Wolverson, D.; Georgiou, T.; Jalil, R.; Novoselov, K. S. *Phys. Rev. B - Condens. Matter Mater. Phys.* **2013**, *87* (8), 1–5.

(5) Wang, L.; Drahushuk, L. W.; Cantley, L.; Koenig, S. P.; Liu, X.; Pellegrino, J.; Strano, M. S.; Bunch, J. S. *Nat. Nanotechnol.* **2015**, *10* (9), 785–790.

(6) Koenig, S. P.; Wang, L.; Pellegrino, J.; Bunch, J. S. *Nat. Nanotechnol.* **2012**, *7* 728-732.

(7) Koenig, S. P.; Boddeti, N. G.; Dunn, M. L.; Bunch, J. S. *Nat. Nanotechnol.* **2011**, *6* (9), 543–546.

(8) Fichter, W. *NASA Tech. Pap.* **1997**, *3658*, 1–24.

(9) Kitt, A. L.; Qi, Z.; Remi, S.; Park, H. S.; Swan, A. K.; Goldberg, B. B. *Nano Lett.* **2013**, *13*, 2605−2610.

(10) Li, S.; Miyazaki, H.; Song, H.; Kuramochi, H.; Nakaharai, S. *ACS Nano* **2012**, 6 (8), 7381–7388.

(11) Carvalho, B. R.; Malard, L. M.; Alves, J. M.; Fantini, C.; Pimenta, M. A. *Phys. Rev. Lett.* **2015**, *114* (13), 1–5.

(12) Liu, H.-L.; Guo, H.; Yang, T.; Zhang, Z.; Kumamoto, Y.; Shen, C.-C.; Hsu, Y.-T.; Li, L.-J.; Saito, R.; Kawata, S. *Phys. Chem. Chem. Phys.* **2015**, *17* (22), 14561–14568.

(13) Feng, J.; Qian, X.; Huang, C.; Li, J. *Nat. Photonics* **2012**, *6* (12), 866–872.